

Sea Ice Loss, Water Vapor Increases, and Their Interactions with Atmospheric Energy Transport in Driving Seasonal Polar Amplification[©]

PO-CHUN CHUNG^a AND NICOLE FELDL^a

^a Department of Earth and Planetary Sciences, University of California, Santa Cruz, Santa Cruz, California

(Manuscript received 7 April 2023, in final form 1 August 2023, accepted 4 August 2023)

ABSTRACT: The ice–albedo feedback associated with sea ice loss contributes to polar amplification, while the water vapor feedback contributes to tropical amplification of surface warming. However, these feedbacks are not independent of atmospheric energy transport, raising the possibility of complex interactions that may obscure the drivers of polar amplification, in particular its manifestation across the seasonal cycle. Here, we apply a radiative transfer hierarchy to an idealized aquaplanet global climate model coupled to a thermodynamic sea ice model. The climate responses and radiative feedbacks are decomposed into the contributions from sea ice loss, including both retreat and thinning, and the radiative effect of water vapor changes. We find that summer sea ice retreat causes winter polar amplification through ocean heat uptake and release, and the resulting decrease in dry energy transport weakens the magnitude of warming. Moreover, sea ice thinning is found to suppress summer warming and enhance winter warming, additionally contributing to winter amplification. The water vapor radiative effect produces seasonally symmetric polar warming via offsetting effects: enhanced moisture in the summer hemisphere induces the summer water vapor feedback and simultaneously strengthens the winter latent energy transport in the winter hemisphere by increasing the meridional moisture gradient. These results reveal the importance of changes in atmospheric energy transport induced by sea ice retreat and increased water vapor to seasonal polar amplification, elucidating the interactions among these physical processes.

KEYWORDS: Atmosphere–ocean interaction; Feedback; Energy transport; Sea ice; Climate change; Climate models

1. Introduction

Both observations (Serreze et al. 2009; Screen and Simmonds 2010a) and simulations forced by increased CO₂ concentrations (Manabe and Wetherald 1975; Holland and Bitz 2003; Hahn et al. 2021) exhibit a strong surface warming in the polar regions as compared with the global average. This phenomenon known as polar amplification is seasonally asymmetric, reaching its maximum during winter and minimum during summer in observations (Serreze et al. 2009; Screen and Simmonds 2010b) and general circulation models (GCMs; Deser et al. 2010; Hahn et al. 2021). Since the projected polar changes are large and are posited to have consequences for global climate, understanding their causes is a central goal of climate science. However, the mechanisms that promote the dramatic seasonality of polar amplification, and the interactions among processes across the seasonal cycle, are still under debate.

Sea ice processes have long been suggested to be the dominant driver of polar amplification via the ice–albedo feedback (Budyko 1969; Manabe and Wetherald 1975; Taylor et al. 2013). Under global warming, sea ice retreat reduces the surface albedo, leading to a greater surface shortwave absorption that warms the polar surface. Additionally, the stable lower

troposphere in the polar region inhibits vertical mixing. The resulting surface-amplified warming produces less outgoing longwave radiation than vertically uniform warming, which requires a strong surface warming to balance the given forcing at the top of atmosphere, a positive lapse rate feedback. At a global scale, the combination of a positive lapse rate feedback at high latitudes and a negative lapse rate feedback at low latitudes indicates a contribution to polar amplification (Pithan and Mauritsen 2014; Goosse et al. 2018; Stuecker et al. 2018; Boeke et al. 2021). Furthermore, since the polar lapse rate feedback is highly correlated to surface warming, some studies emphasize the combined mechanism of the positive lapse rate feedback and ice–albedo feedback (Graversen et al. 2014; Feldl et al. 2017, 2020). Notably, these feedbacks operate in different seasons and are linked by seasonal ocean heat storage and release (Boeke and Taylor 2018; Dai et al. 2019; Feldl et al. 2020; Shaw and Smith 2022) and changes in effective surface heat capacity as melting ice transitions to open ocean (Manabe and Stouffer 1980; Dwyer et al. 2012; Hahn et al. 2022).

Preferential increases in tropical humidity amplify warming in the tropics relative to the high latitudes, thus acting against polar amplification. Nevertheless, polar increases in water vapor promote polar warming, and that warming may in turn activate other feedbacks. Results from a single column model suggest that the water vapor feedback induced by increased specific humidity from remote sources produces considerable near-surface warming in high latitudes (Henry et al. 2021), which would manifest as a positive lapse rate feedback. Similarly, in a moist energy balance model, the water vapor feedback amplifies other positive feedbacks in the polar region,

[©] Supplemental information related to this paper is available at the Journals Online website: <https://doi.org/10.1175/JCLI-D-23-0219.s1>.

Corresponding author: Po-Chun Chung, pochung@ucsc.edu

thus rising to predominance in driving polar amplification (Beer and Eisenman 2022). Through idealized modeling, these studies suggest the role of water vapor in polar amplification may be underappreciated: interactions among the water vapor feedback and other processes promote polar warming regardless of the meridional structure of the feedback considered in isolation.

Although diagnostics applied to coupled model experiments indicate that the total atmospheric heat transport makes small contributions to polar amplification (Pithan and Mauritsen 2014; Goosse et al. 2018), the dry and moist components of energy transport changes are large and compensating (Stuecker et al. 2018; Graversen and Langen 2019; Feldl et al. 2020; Hahn et al. 2021; Henry et al. 2021; Taylor et al. 2022). Idealized model experiments have shown that a stronger surface polar heat source, such as associated with a stronger surface albedo feedback, produces a stronger decrease in poleward dry energy transport, offsetting polar warming (Feldl et al. 2017; Henry et al. 2021). This is consistent with the well-known anticorrelation between polar amplification and changes in atmospheric energy transport (Hwang et al. 2011). On the other hand, an increase in latent energy transport may have an outsized warming impact on the polar regions via the “water vapor triple effect,” which includes the greenhouse effect of increased moisture and cloudiness, as well as the latent heat release of water vapor condensation (Graversen and Burtu 2016; Baggett and Lee 2017; Yoshimori et al. 2017; Graversen and Langen 2019; Taylor et al. 2022, their Fig. 12). Slightly counteracting this warming effect, a strong increase in the moist component of energy transport, and a weak decrease in the dry component, reduces the polar lapse rate feedback (Feldl et al. 2020).

While these prior works suggest an underappreciated polar warming role for water vapor and the moist component of atmospheric energy transport, it remains unclear how they manifest across the seasonal cycle and interact with the ice–albedo and lapse rate feedback. Here we use an idealized GCM coupled to a thermodynamic sea ice model as a minimal model for probing the mechanism of seasonal polar amplification, including the crucial effects of radiative feedbacks, sea ice retreat and thinning, and atmospheric energy transport. Aquaplanet simulations with thermodynamic sea ice, though relatively unexplored, have yielded important insights about the seasonality of polar amplification (Feldl and Merlis 2021) and the midlatitude storm track response to sea ice loss (Shaw and Smith 2022). We further advance the model configuration by pairing it with a radiative transfer hierarchy to isolate the roles of water vapor increases and sea ice loss, as well as their interactions with atmospheric energy transport across the seasonal cycle in driving polar amplified warming.

2. Models and method

a. Models and experimental design

We use the Isca modeling framework (Vallis et al. 2018), based on the Geophysical Fluid Dynamics Laboratory (GFDL) dynamical core. The resolution of the atmospheric component is T42 ($\sim 2.8^\circ \times 2.8^\circ$) with 30 evenly spaced vertical levels, and

it is coupled to a thermodynamic sea ice model following Zhang et al. (2022) and a 60-m mixed layer slab ocean. The convection scheme is a simplified Betts–Miller scheme described in Frierson et al. (2007). The insolation includes a seasonal cycle of a 360-day year with the equinoxes at days 90 and 270 but no diurnal cycle. The solar constant is 1360 W m^{-2} , with a circular Earth’s orbit (eccentricity = 0) and an Earth-like obliquity of 23.439° . Our model configuration is an idealized aquaplanet with no clouds, no continents, and no ocean heat transport (i.e., Q flux is zero). All experiments in this study are run for 70 years with 30 years of spinup.

To investigate the role of the water vapor feedback, we conduct experiments with a hierarchy of radiative transfer schemes: gray radiation and Rapid Radiative Transfer Model (RRTM). The gray radiation scheme follows Frierson et al. (2006), in which longwave optical depth depends on latitude ϕ and pressure p :

$$\tau_0 = \tau_e + (\tau_p - \tau_e) \sin^2 \phi, \quad \tau = \tau_0 \left[f_1 \frac{P}{P_s} + (1 - f_1) \left(\frac{P}{P_s} \right)^4 \right], \quad (1)$$

where τ_e and τ_p are surface values of longwave optical depth at the equator and pole, respectively; f_1 is the linear absorption factor; and P_s is the surface pressure. We tune the gray radiation parameters to achieve the same climatology as the RRTM simulations. Specifically, optical depth parameters are set to $(\tau_p, \tau_e) = (2.5, 5.8)$, and $f_1 = 0.2$. A top-of-atmosphere (TOA) co-albedo profile, $0.7535 - 0.0345[(3 \sin^2 \phi - 1)/2]$, is applied to the insolation to scale the TOA net shortwave flux to match that in RRTM. The global warming scenario is simulated by multiplying τ_0 by a tuning value of 1.155 to reproduce the radiative forcing in the $4 \times \text{CO}_2$ scenario in RRTM. For the RRTM radiative transfer scheme (Mlawer et al. 1997), we follow the setup of the Model of an Idealized Moist Atmosphere (MiMA; Jucker and Gerber 2017). Importantly, since the calculations of radiative heating are based on the atmospheric temperature and humidity structure, this model includes a water vapor feedback. The CO_2 concentration is 300 ppm in the control run. We perform the global warming scenario by quadrupling the CO_2 concentration. The magnitude of the radiative forcings in the gray radiation and RRTM schemes are 9.29 and 9.28 W m^{-2} , respectively, calculated as the TOA radiative flux change in the perturbation simulations relative to simulations with the surface boundary fixed (i.e., the fixed-SST forcing; Hansen et al. 2005).

We implement sea ice thermodynamics from Zhang et al. (2022), which is based on Semtner (1976), in our slab ocean boundary rather than the Isca default prescribed sea ice representation, in which ice distribution does not depend on atmospheric or oceanic temperature. The sea ice thickness h_i is governed by the following equation:

$$L_i \frac{dh_i}{dt} = F_{\text{atm}} - F_{\text{base}}, \quad (2)$$

where $L_i = 3.0 \times 10^8 \text{ J m}^{-3}$ is latent heat of fusion of ice; F_{atm} is the net energy flux exchange between surface and atmosphere,

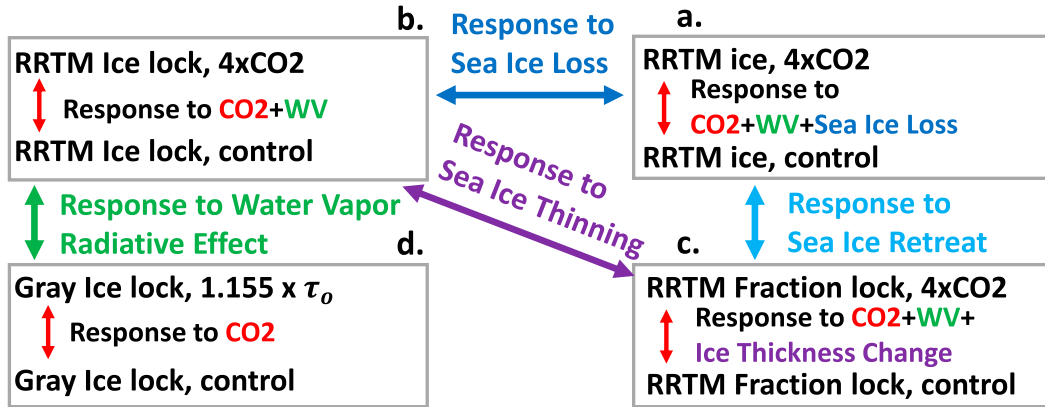


FIG. 1. The schematic of simulations. Boxes referred to in the main text are labeled as a–d.

including radiative, sensible, and latent heat fluxes (F_{rad} , F_{SH} , and F_{LH} , respectively); and F_{base} is the basal heat flux from the ocean mixed layer into the ice. The F_{base} depends linearly on the temperature gradient between the mixed layer (T_{ml}) and the ice base (freezing point $T_{\text{base}} = 273.15 \text{ K}$): $F_{\text{base}} = F_0(T_{\text{ml}} - T_{\text{base}})$, where $F_0 = 120 \text{ W m}^{-2} \text{ K}^{-1}$ is the ocean–ice heat exchange coefficient. The ocean mixed-layer temperature T_{ml} is determined by

$$\rho_w c_w h_{\text{ml}} \frac{dT_{\text{ml}}}{dt} = \begin{cases} -F_{\text{base}} & \text{where ice is present} \\ -F_{\text{atm}} & \text{under ice-free condition} \end{cases}, \quad (3)$$

where $\rho_w = 1035 \text{ kg m}^{-3}$ is the density of seawater, $c_w = 3989.24 \text{ J kg}^{-1} \text{ K}^{-1}$ is the specific heat of water, and $h_{\text{ml}} = 60 \text{ m}$ is the ocean mixed layer depth. When ice is present, conductive heat flux through ice F_i is given by

$$F_i = k_i \frac{T_{\text{base}} - T_s}{h_i}, \quad (4)$$

and the surface temperature T_s is determined by a balance between the surface flux F_{atm} , which is a function of T_s , and the conductive heat flux through the ice F_i :

$$F_{\text{rad}} + F_{\text{SH}} + F_{\text{LH}} = k_i \frac{T_{\text{base}} - T_s}{h_i}, \quad (5)$$

where $k_i = 2 \text{ W m}^{-1} \text{ K}^{-1}$ is the thermal conductivity of sea ice. Last, ice fraction f_{ice} is set to 1 where the ice thickness h_i is greater than 0 and is set to 0 elsewhere. The surface albedo is a linear function of ice fraction: $\alpha = (1 - f_{\text{ice}})\alpha_{\text{ocn}} + f_{\text{ice}}\alpha_{\text{ice}}$; we use values of ocean and ice albedo ($\alpha_{\text{ocn}}, \alpha_{\text{ice}} = (0.22, 0.45)$).

In addition to the fully interactive sea ice thermodynamics implementation described above, we apply the direct ice-nudging method to lock the ice thickness (and fraction) to deactivate sea ice loss, and lock only the ice fraction to disable the sea ice–albedo feedback. Ice fraction-locked simulations are run for RRTM control and forced CO₂. Ice thickness-locked simulations are run for both radiation models (RRTM and gray) and for both control (CTL) and perturbation (PTB; forced CO₂ or optical depth) configurations. All locking experiments are locked at every model time step to the ice

thickness and fraction from the RRTM control simulation with interactive sea ice. These eight simulations, illustrated schematically in Fig. 1, enable us to isolate different physical components of the forced climate response. The total response is composed of the response to CO₂, the water vapor radiative effect (WV), and interactive sea ice loss (box a; RRTM_{ice}PTB – RRTM_{ice}CTL). The response to CO₂ and WV in the absence of ice loss (box b) is RRTM_{ice-lock}PTB – RRTM_{ice-lock}CTL. The response to CO₂, WV, and ice thickness changes (box c) is RRTM_{fraction-lock}PTB – RRTM_{fraction-lock}CTL. The response to CO₂ (box d) is Gray_{ice-lock}PTB – Gray_{ice-lock}CTL. All of these responses occur in the presence of temperature feedbacks (Planck and lapse rate).

The response to WV and sea ice loss in isolation from radiative forcing can then be determined by box b – box d and box a – box b, respectively. Strictly, the response to the water vapor radiative effect will also include any differences in temperature feedbacks between RRTM and the gray radiation schemes. The temperature feedbacks in RRTM_{ice-lock} are close to that in Gray_{ice-lock} in the polar regions but about 61% weaker (less negative) in the tropics (Fig. S1 in the online supplemental material), comparable in magnitude to the water vapor feedback itself in the tropics. However, as detailed below in section 2b, the warming contributions associated with each feedback are calculated as the radiative response normalized by the global-mean Planck feedback and, in sections 3b and 3c, we will demonstrate that the contributions of the temperature feedbacks are within 0.5 K in both radiative schemes. The response to sea ice loss can further be decomposed into a response to sea ice retreat and the response to sea ice thinning, determined by box a – box c and box c – box b, respectively. The response to sea ice thinning arises due to the difference between two experiments with locked ice fraction, but in one, ice thickness is free to change. The response to sea ice retreat captures the effect of albedo change in the absence of ice thickness change.

We note that sea ice interventions typically neglect to conserve energy or freshwater and have been shown to impose artificial heating in an idealized model (England et al. 2022). Given the present study's specific objective of fixing ice fraction, and ice fraction and thickness, the ice-nudging method is

the most straightforward approach. Nudging the ice to remain at its climatological state disables a latent heating mechanism, and we will show that this leads to a larger surface warming in summer than the simulations with interactive ice. We posit that this surplus warming is physically meaningful; in addition to the radiative feedbacks associated with sea ice retreat, the absorption of latent heat by melting ice influences the surface temperature response, and we quantify this effect via mechanism denial. Moreover, since the component responses sum to the total response with interactive sea ice—by construction with no residual—this effect is part of the total response.

b. Warming contribution method

The local atmospheric energy balance is used to quantify the contribution of physical mechanisms to spatial patterns of warming (Feldl and Roe 2013; Pithan and Mauritsen 2014; Goosse et al. 2018; Stuecker et al. 2018; Hahn et al. 2021):

$$F + (\lambda_p + \sum_i \lambda_i) \delta T_s + \delta \text{AHT}_d + \delta \text{AHT}_q + \delta \text{SEB} + \delta R_{\text{res}} = 0. \quad (6)$$

It includes radiative forcing F , the radiative response associated with the Planck feedback $\lambda_p \delta T_s$ and with other climate feedbacks $\lambda_i \delta T_s$, anomalous dry and moist components of atmospheric heat transport (δAHT_d and δAHT_q), anomalous surface energy budget (δSEB), and a residual term (δR_{res}), all in units of watts per meter squared. As a reminder, there is no ocean heat transport in the aquaplanet and hence no associated warming contribution. The warming contributions are obtained by dividing each term in Eq. (6) by the global- and annual-mean Planck feedback $\overline{\lambda_p}$ ($\text{W m}^{-2} \text{K}^{-1}$):

$$\delta T_s = -\frac{F}{\overline{\lambda_p}} - \frac{\lambda'_p \delta T_s}{\overline{\lambda_p}} - \frac{\sum_i \lambda_i \delta T_s}{\overline{\lambda_p}} - \frac{\delta \text{AHT}_d}{\overline{\lambda_p}} - \frac{\delta \text{AHT}_q}{\overline{\lambda_p}} - \frac{\delta \text{SEB}}{\overline{\lambda_p}} - \frac{\delta R_{\text{res}}}{\overline{\lambda_p}}, \quad (7)$$

where $\lambda'_p = \lambda_p - \overline{\lambda_p}$ is the departure of the Planck feedback from its global, annual mean. The surface energy budget term is given by the change in surface radiative and turbulent energy fluxes and represents, in the aquaplanet, changes in ocean heat uptake. We calculate the monthly contributions for each term. The winter is defined as December–February (DJF) for the northern polar regions (60° – 90°), while the summer is defined as June–August (JJA). The range of tropics is within 30° .

Climate feedbacks are calculated using the radiative kernel method (Shell et al. 2008; Soden et al. 2008), which decomposes the changes in TOA radiation into the contribution of individual climate variables. We calculate a temperature kernel for the gray radiation scheme and, separately, temperature and water vapor kernels for RRTM. Each kernel calculation is based on the respective control climate with interactive sea ice simulated at $8 \times$ daily resolution. Temperature is perturbed by 1 K in each atmospheric layer and at the surface, and specific humidity by the logarithm of the anomaly corresponding

to a 1-K warming, assuming constant relative humidity. The resulting monthly kernels are weighted by the pressure thickness of each layer relative to 100 hPa, such that the units are $\text{W m}^2 \text{K}^{-1}$ (100 hPa) $^{-1}$. The ice–albedo feedback is calculated using the approximate partial radiative perturbation (APRP) method (Taylor et al. 2007) instead of the kernel method.

Following Donohoe et al. (2020), the seasonal total atmospheric heat transport (AHT) is calculated by the difference between monthly TOA and surface energy fluxes:

$$\text{AHT}(\phi) = 2\pi a^2 \int_{-(\pi/2)}^{\phi} (F_{\text{TOA}} - F_{\text{sfc}} - \text{storage}_{\text{atm}}) \cos \phi' d\phi', \quad (8)$$

where F_{TOA} and F_{sfc} are downward TOA radiative flux and the surface energy flux, respectively; and a is the radius of Earth. The atmospheric energy storage term ($\text{storage}_{\text{atm}}$) is governed by the vertical integral of sensible and latent heat:

$$\text{storage}_{\text{atm}} = \frac{1}{g} \int_0^{P_s} \frac{d}{dt} (c_p T + Lq) dp, \quad (9)$$

where c_p is the specific heat of air at constant pressure and L is the latent heat of vaporization. The seasonal moist atmospheric heat transport (AHT_q) is calculated by monthly evaporation E minus precipitation P :

$$\text{AHT}_q(\phi) = 2\pi a^2 \int_{-(\pi/2)}^{\phi} L(E - P - \text{storage}_{\text{atm},q}) \cos \phi' d\phi', \quad (10)$$

where

$$\text{storage}_{\text{atm},q} = \frac{1}{g} \int_0^{P_s} \frac{dq}{dt} dp. \quad (11)$$

The dry component is determined by the difference between total and moist AHT:

$$\text{AHT}_d(\phi) = \text{AHT}(\phi) - \text{AHT}_q(\phi). \quad (12)$$

The global mean value of each term in Eqs. (8) and (10) is removed to ensure zero transport at poles.

3. Results

a. Warming pattern and its seasonality

The anomalous air temperature is decomposed into the warming associated with CO_2 , with the water vapor radiative effect, and with sea ice loss (Fig. 2). In the annual mean, the total response (Fig. 2a) presents a classic global warming pattern, including tropical warming in the upper troposphere and polar amplification. The former is mainly contributed by the response to the water vapor radiative effect (Fig. 2c), and the latter is mainly contributed by the response to sea ice loss (Fig. 2d). The response to sea ice loss (Fig. 2d) is dominated by the response to sea ice retreat (Fig. 2e), which presents a strong surface-amplified and polar-amplified warming. By construction,

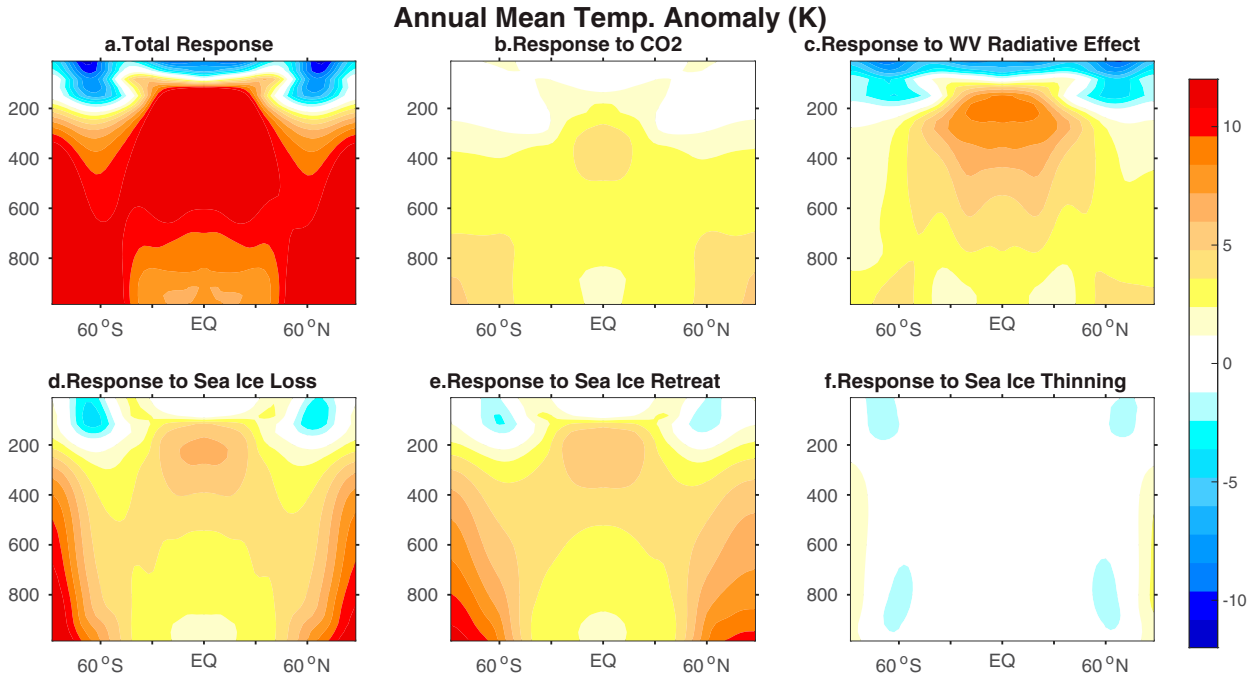


FIG. 2. Zonal and annual mean atmospheric temperature response (K) to (a) all drivers, (b) CO₂, (c) water vapor radiative effect, (d) sea ice loss, (e) sea ice retreat, and (f) sea ice thinning.

the individual responses add to the total response with no residual warming. Figure 3 shows the seasonal anomalous surface temperature. As expected, the surface manifestation of the polar-amplified atmospheric warming occurs during winter

(Fig. 3a). Since the responses to CO₂ and water vapor radiative effect (Figs. 3b,c) have no apparent change throughout the seasonal cycle, the seasonality of polar amplification is dominated by the response to sea ice loss (Fig. 3d).

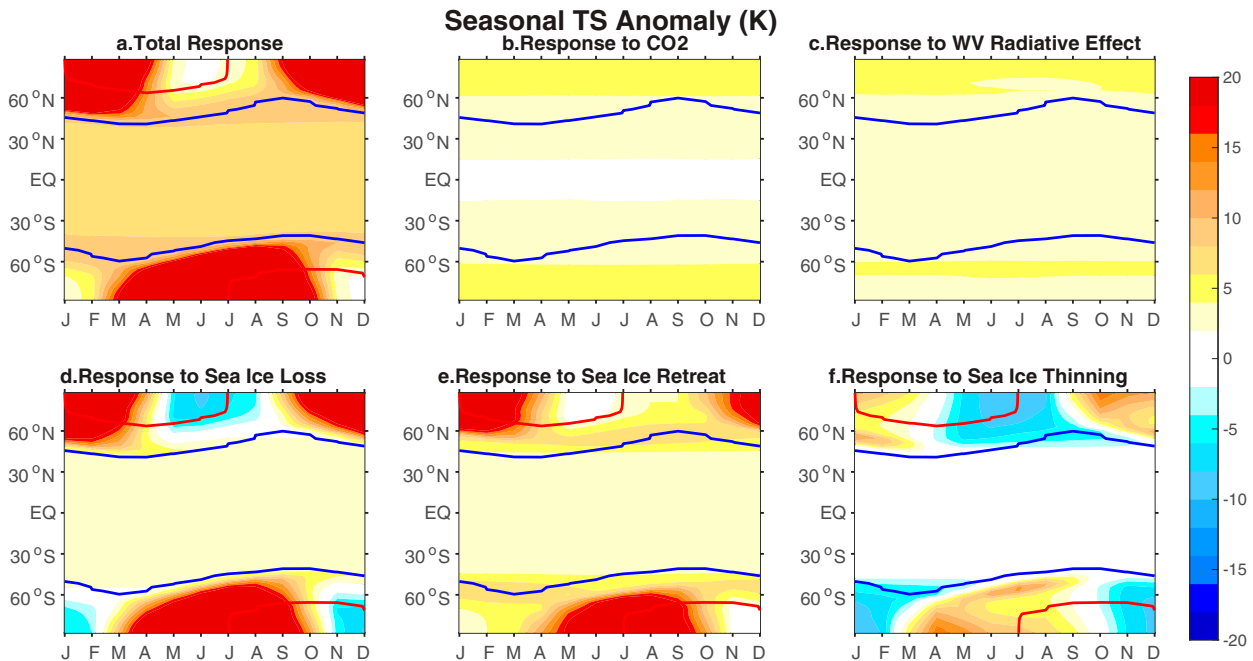


FIG. 3. Zonal mean seasonal surface temperature response (K) to (a) all drivers, (b) CO₂, (c) water vapor radiative effect, (d) sea ice loss, (e) sea ice retreat, and (f) sea ice thinning. Solid contours show the ice edge, defined where ice fraction is marginally nonzero (i.e., 1%), in the RRTM_{ice} control (blue) and 4 × CO₂ (red) simulations.

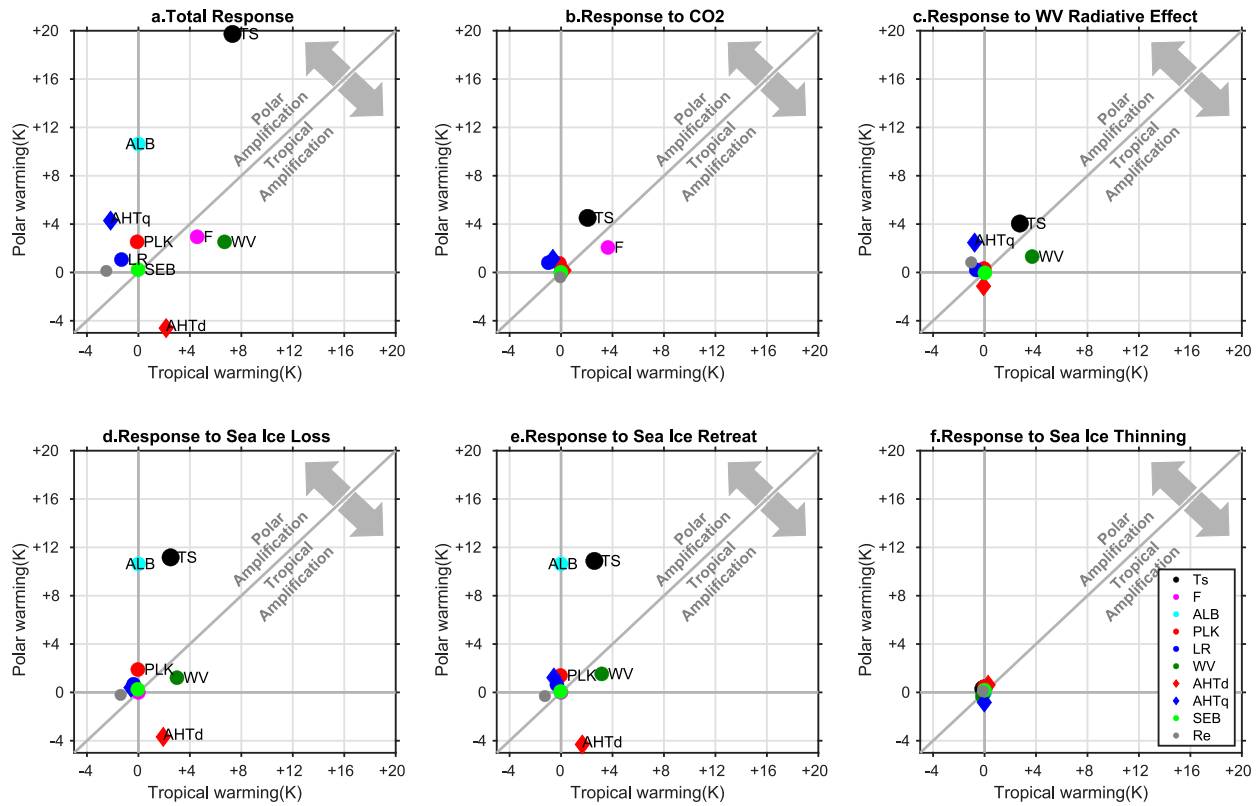


FIG. 4. Annual mean warming contributions (K) to (a) the total surface temperature change and the surface temperature change due to (b) CO₂, (c) water vapor radiative effect, (d) sea ice loss, (e) sea ice retreat, and (f) sea ice thinning. Warming contributions are shown for forcing (*F*), albedo feedback (ALB), Planck feedback (PLK), lapse rate feedback (LR), water vapor feedback (WV), change in dry and moist atmospheric heat transport (AHT_d and AHT_q, respectively), surface energy budget (SEB), and residual term (Re). The contributors above and below the one-to-one line contribute to polar and tropical amplification, respectively. The polar region is defined as 60°–90°N, and the tropical region is defined within 30°.

The asymmetric surface temperature pattern includes summertime cooling and wintertime warming, which is composed of the response to sea ice retreat and response to sea ice thinning. The strong wintertime polar amplification presented in response to sea ice retreat (Fig. 3e) is initiated by ice-albedo feedback, which will be discussed in section 3c. The response to sea ice thinning (Fig. 3f) presents summer cooling and winter warming. In summer, latent heating associated with sea ice melt is expected to inhibit the surface warming. The ice-locking simulation excludes this physical process, allowing a greater temperature increase with CO₂ forcing. Thus, the difference between the simulation in which only ice fraction is locked and the simulation in which ice thickness and fraction are locked presents a summer cooling response. In winter, for the surface temperature below the freezing point, increased conductive heat flux caused by thinning ice (not shown) results in surface warming, consistent with Hahn et al. (2022). The latent heat absorption by melting ice and increased conduction through thinner ice together explain the asymmetric seasonality of polar surface temperature when the climate warms.

b. Annual mean warming contribution

To thoroughly investigate the detailed mechanisms of polar amplification characterized in the previous section, we use the

warming contribution method (see section 2b). Figure 4 shows the annual mean warming contributions associated with individual feedbacks and atmospheric energy transports, with the total warming indicated by the black marker. The dominant contributor to the total response is the ice-albedo feedback (Fig. 4a); in addition, the latent energy transport contributes strongly to polar warming. The water vapor feedback and dry energy transport contribute to tropical warming. Unlike previous studies that consider lapse rate feedback a primary role in polar amplification (Pithan and Mauritsen 2014; Goosse et al. 2018; Stuecker et al. 2018; Boeke et al. 2021), it contributes little in our simulations. Consistent with this modest contribution, the vertical warming structure (Fig. 2a) in our model is relatively uniform throughout the polar troposphere. Though the warming profile is bottom-heavy in DJF (Fig. S2 in the online supplemental material), which would be expected to promote a positive lapse rate feedback, the RRTM radiative kernel in that season is weak (not shown) and hence lower tropospheric warming has little impact of the TOA radiative flux. The weak kernel is likely related to the idealizations of our model, in particular the lack of clouds. The warming profile is top-heavy in JJA (Fig. S2), producing a seasonally negative lapse rate feedback.

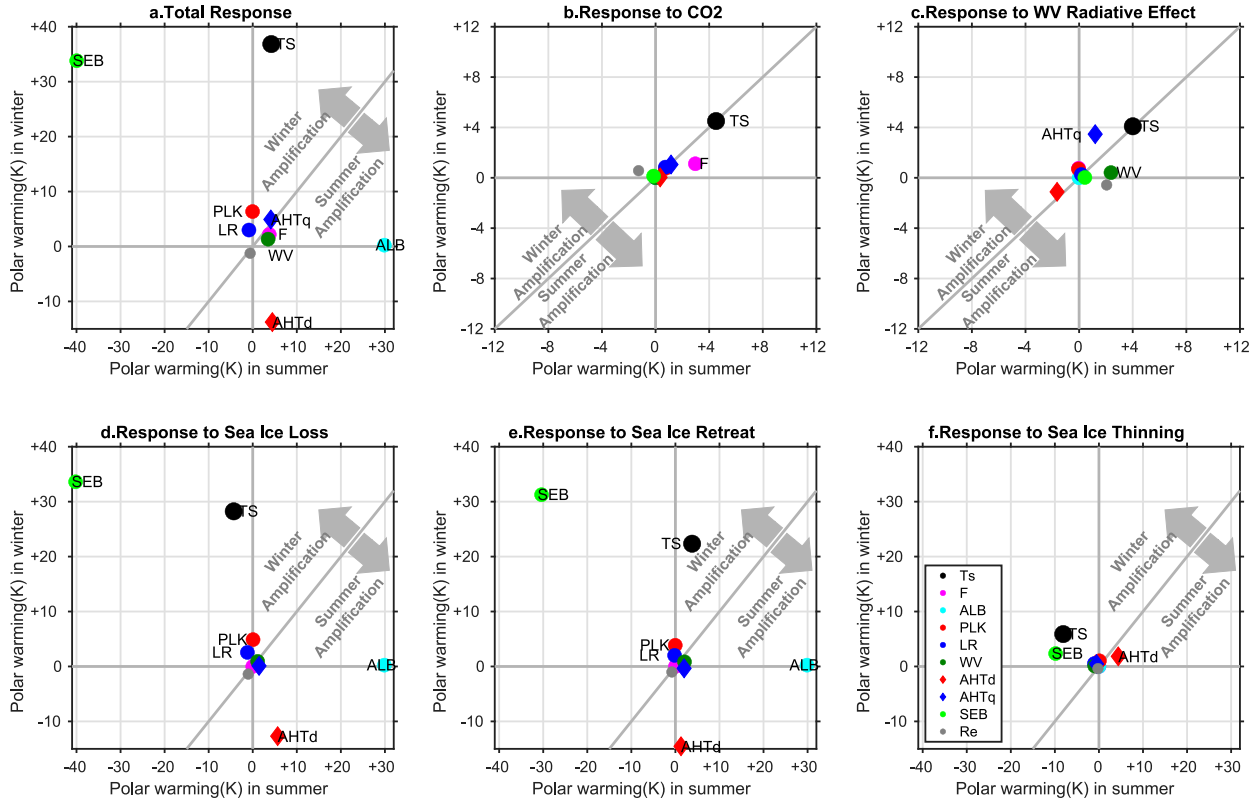


FIG. 5. Similar to Fig. 4, but for seasonal warming contribution (K) to the polar surface temperature change. The contributors above and below the one-to-one line contribute to winter and summer amplification, respectively. Note that the axes in (b) and (c) are different from the others.

The tropical amplification due to the water vapor primarily comes from the response to water vapor radiative effect, as does the increase in poleward latent energy transport (Fig. 4c). Physically, increased water vapor in the tropics supports both a tropically amplified water vapor feedback and an increase in poleward latent energy transport via an enhanced meridional humidity gradient. Although the water vapor feedback contributes to tropical warming, the increasing poleward latent energy transport contributes to polar warming concomitantly. Hence, the combination of the two causes a nearly uniform surface warming that slightly supports polar amplification. Moreover, the Planck and lapse rate feedbacks contribute negligibly here, illustrating that the main difference between RRTM and gray radiative schemes is dominated by the water vapor radiative effect rather than temperature feedbacks, as mentioned in section 2a.

Sea ice loss (Fig. 4d) is the primary physical mechanism leading to polar amplification. The ice-albedo feedback plays the predominant role in polar amplification while the decreased poleward dry transport, consistent with the reduced meridional temperature gradient, contributes to tropical amplification. In addition, the enhanced water vapor feedback slightly supports tropical warming because of the strong moistening for a given warming in higher initial temperature regions from the Clausius-Clapeyron relation. In comparing Figs. 4e and 4f, we confirm that, in the annual mean, the mechanisms that produce surface warming in response to sea ice loss arise

entirely from sea ice retreat. Sea ice thinning activates no annual-mean feedbacks.

c. Seasonal warming contribution

The seasonal polar warming contributions are calculated to identify the processes that promote polar amplification as a wintertime phenomenon (Fig. 5). In the total response (Fig. 5a), an increase in upward surface energy fluxes leads to winter warming. In contrast, the ice-albedo feedback and dry energy transport are the main contributors to summer amplification, and the rest of the contributors play a minor role. This pattern of the surface energy budget overcompensating the ice-albedo feedback and dry energy transport arises from the response to sea ice loss (Fig. 5d), and specifically the response to sea ice retreat (Fig. 5e). Physically, the ice-albedo feedback contributes to summer warming; however, it is balanced by ocean heat uptake, and the release of energy back to the atmosphere results in polar amplification during winter. The mechanism of seasonal ocean storage and release triggered by summertime ice-albedo feedback has also been found in fully coupled models (Feldl et al. 2020; Hahn et al. 2021; Jenkins and Dai 2021). The decrease in dry energy transport stems from the reduced meridional temperature gradient associated with wintertime polar warming.

The surface energy budget in the polar region (poleward of 60°N) is further decomposed to provide insights into the mechanisms of seasonal ocean-atmosphere exchange associated

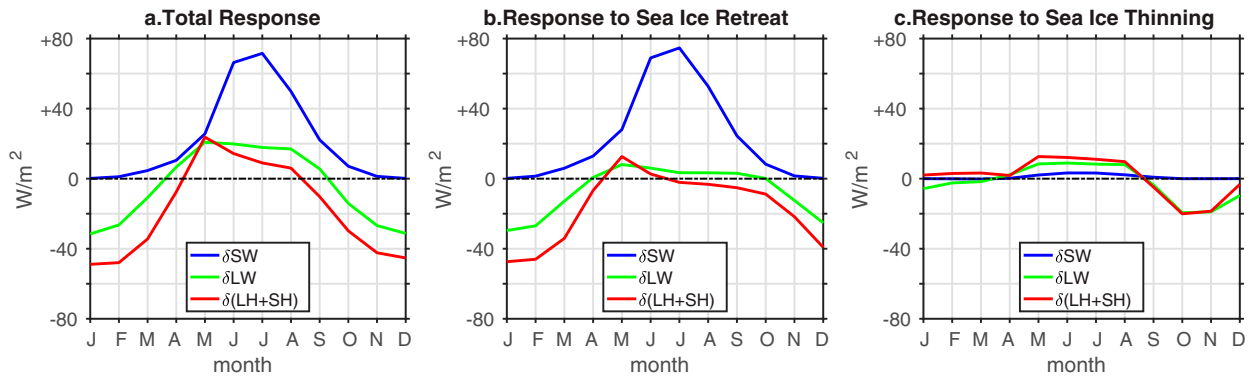


FIG. 6. The decomposition of seasonal surface energy budget (W m^{-2}) response to (a) all drivers, (b) sea ice retreat, and (c) sea ice thinning in the polar region. The surface energy budget comprises shortwave (SW; blue), longwave (LW; green), and turbulent heat flux (latent and sensible heat: LH+SH; red). Downward is defined as positive.

with sea ice loss (Fig. 6). When sea ice retreats, the ocean absorbs a large amount of surface shortwave flux during summer (blue line in Fig. 6b) and releases heat during winter. The enhanced winter warming heats the lower atmosphere through both turbulent heat flux (latent and sensible heat flux) and longwave radiation. The seasonal surface energy budget response to sea ice loss is consistent with the ECHAM6 slab ocean model (Shaw and Smith 2022) and CESM1 coupled model (Jenkins and Dai 2021). In contrast, sea ice thinning has no equivalent shortwave absorption, and the small summer downward and winter upward anomalous longwave and turbulent heat flux (Fig. 6c) are induced by the summer cooling and winter warming pattern in response to sea ice thinning. Specifically, the response to sea ice thinning produces moderate winter amplification stemming from the surface energy balance term (Fig. 5f), which is consistent with an increased conductive heat flux through ice in winter and suppressed warming in summer. As discussed in section 3a, the suppression of summer warming manifests here as a surface cooling because of the strong warming in the ice-locking simulations. Summer cooling also slightly increases the poleward dry energy transport.

The seasonal response to water vapor radiative effect (Fig. 5c) is much smaller than that to sea ice loss (note the different axes in Figs. 5b,c). Intriguingly, the cancellation between the water vapor feedback and latent energy transport previously identified in the annual mean analysis is also evident in the seasonal polar warming. We interpret this in terms of seasonal vertically integrated atmospheric humidity changes in response to the water vapor radiative effect. As shown in Fig. 7, the water vapor changes feature enhanced moisture in summer and an increased meridional humidity gradient in winter. The change in meridional humidity gradient at 60°N is $0.0041 \text{ g m}^{-2} \text{ km}^{-1}$ in DJF, as compared with $0.0023 \text{ g m}^{-2} \text{ km}^{-1}$ in JJA. Although the water vapor feedback and increased latent energy transport warm the polar regions in all seasons, the former is stronger in summer than winter, while the latter is stronger in winter than summer, leading to no seasonal asymmetry in polar warming in response to water vapor radiative effect (black circle in Fig. 5c falls on 1:1 line). From a global perspective, this response is

tied to the seasonal progression of humidity changes, as the moistening tropics shift poleward toward the summer hemisphere and away from the winter hemisphere. Last, the seasonal contributions of Planck and lapse rate feedbacks are extremely small, as mentioned in section 2a and consistent with our interpretation of this response as due to the water vapor radiative effect.

d. Energy transport

To further understand the role of remote interactions with polar amplification, the annual mean and seasonal atmospheric energy transport are diagnosed. Figure 8 shows the annual mean northward atmospheric energy transport. In the total response (Fig. 8a), the total poleward atmospheric energy transport into the polar regions (60°) is close to zero, with dry and moist components tending to compensate one another, consistent with Hwang et al. (2011) and Graversen and Langen (2019), even without oceanic energy transport in our models. By separating the atmospheric heat transport into component responses, we find that the CO_2 and water vapor radiative effect (Figs. 8b,c) explain the increase in total heat transport, and the sea ice retreat (Fig. 8e) explains

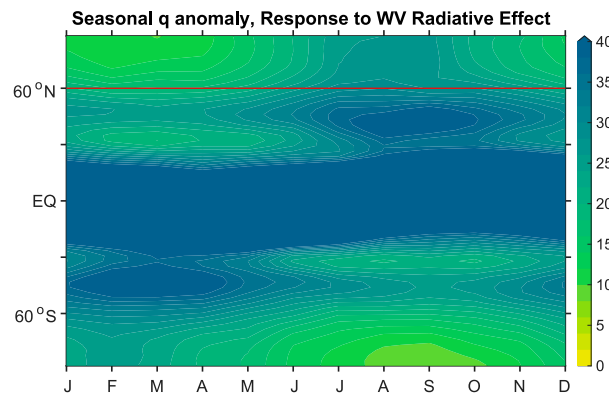


FIG. 7. Zonal mean seasonal vertically integrated specific humidity (g m^{-2}) response to water vapor radiative effect. The horizontal line marks 60°N .

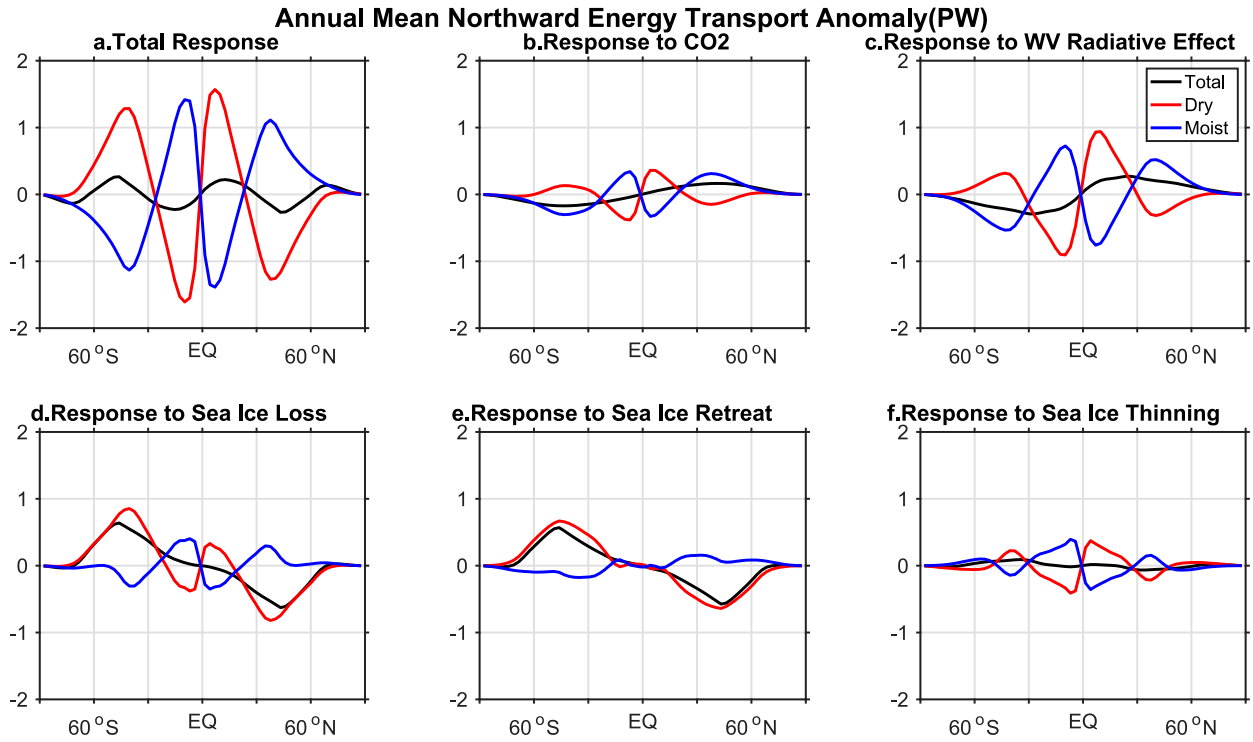


FIG. 8. Annual mean northward atmospheric energy transport (PW) response to (a) all drivers, (b) CO₂, (c) water vapor radiative effect, (d) sea ice loss, (e) sea ice retreat, and (f) sea ice thinning. Total, dry component, and moist component are shown with black, red, and blue, respectively.

the decrease. This behavior is due to an overcompensation by the latent energy transport in response to CO₂ and water vapor radiative effect and an overcompensation by the dry energy transport in response to sea ice retreat. [Audette et al. \(2021\)](#) further explain the decrease in poleward heat transport in response to sea ice loss as a warming of the returning moist isentropic circulation at high latitudes, while sea surface warming instead strengthens the moist isentropic circulation and hence poleward heat transport. Sea ice thinning does not strongly impact annual-mean poleward energy transport (Fig. 8f).

Figures 9 and 10 show the seasonal poleward dry and moist components of atmospheric heat transport. The seasonality of dry energy transport in the total response (Fig. 9a) in the mid- to high latitudes arises from the response to sea ice loss (Fig. 9d), with a substantial winter decrease associated with sea ice retreat (Fig. 9e) and a summer increase and winter decrease associated with sea ice thinning (Fig. 9f). The seasonal pattern of dry energy transport is highly connected to the seasonal warming pattern. The strong winter weakening in response to sea ice retreat results from the strong winter amplification of polar warming (Fig. 3e). The weaker summer strengthening and winter weakening in response to sea ice thinning trace back to the weaker summer cooling and winter warming (Fig. 3f). In sum, the dry energy transport changes can be interpreted in terms of the seasonal polar warming in a straightforward manner. For total changes in latent energy transport (Fig. 10a), the seasonality in the mid- to high latitudes

is dominated by the water vapor radiative effect (Fig. 10c). In particular, the slight winter maxima that emerges in the absence of sea ice loss is consistent with the seasonally enhanced meridional moisture gradient (Fig. 7) and is also apparent in the change in northward energy transport at 60°N (Fig. S3 in the online supplemental material).

4. Summary and discussion

We use the Isca modeling framework ([Wallis et al. 2018](#)) coupled to a thermodynamic sea ice model ([Semtner 1976](#); [Zhang et al. 2022](#)) to investigate the cause of polar amplification forced by increased greenhouse gas concentrations. By comparing the model with different radiative schemes and sea ice locked to its seasonally varying climatological control state, we separate the total climate response into the response to CO₂, water vapor radiative effect, sea ice retreat, and sea ice thinning. Furthermore, for each response, a feedback analysis is performed to quantify the warming contributions associated with particular physical processes, such as the ice–albedo feedback, the water vapor feedback, ocean heat uptake, and dry and latent atmospheric energy transports.

The ice–albedo feedback plays the dominant role in polar amplified warming. The summertime ice–albedo feedback contributes to wintertime polar amplification through ocean heat uptake and release. Accompanied by the exposed ocean, the enhanced upward longwave and turbulent heat flux during

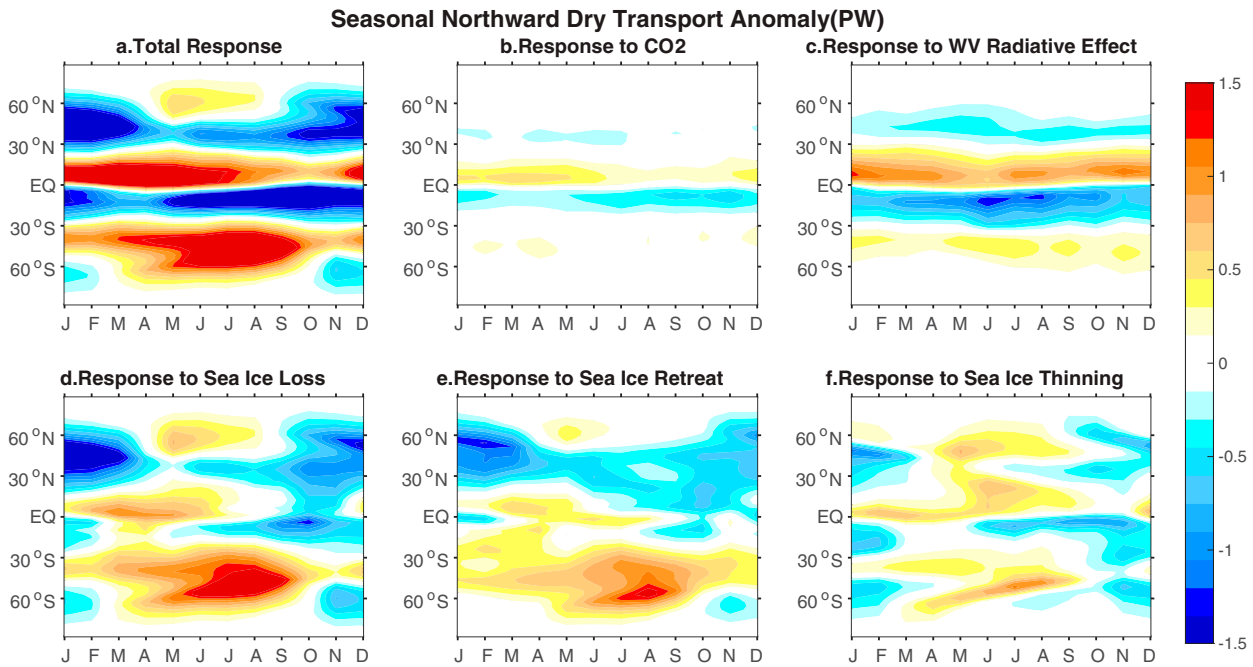


FIG. 9. Seasonal northward dry component of atmospheric energy transport (PW) response to (a) all drivers, (b) CO₂, (c) water vapor radiative effect, (d) sea ice loss, (e) sea ice retreat, and (f) sea ice thinning.

winter heats the lower troposphere and induces a strong decrease in poleward dry energy transport and a weakly positive polar lapse rate feedback. The minor contribution of the lapse rate feedback to polar warming, in contrast to previous studies (Pithan and Mauritsen 2014; Goosse et al. 2018; Stuecker et al. 2018; Boeke et al. 2021), likely results from more

uniform atmospheric warming in our idealized model and a weak TOA radiative response to that warming (i.e., a weak temperature kernel). A more realistic lapse rate feedback may support a stronger polar amplification via the response to sea ice retreat, especially in winter, offset to some extent by a correspondingly larger decrease in dry energy transport.

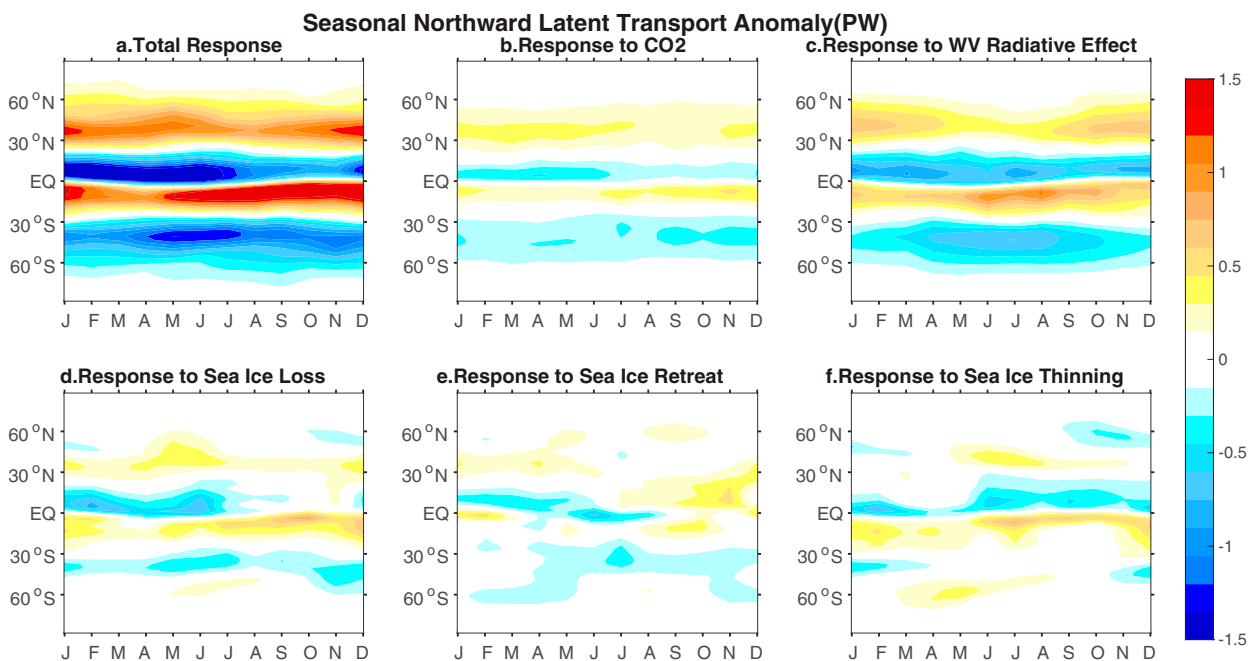


FIG. 10. As in Fig. 9, but for moist component.

However, we do not expect it to become a strong contributor to the response to water vapor radiative effect, which exhibits only modest surface-amplified warming in high latitudes (Fig. 2c). Overall, these ocean-atmosphere coupled mechanisms are consistent with previous studies: The seasonal polar amplification is supported by a more positive winter lapse rate feedback (Boeke et al. 2021; Feldl et al. 2020) and reduced by a decreasing poleward dry energy transport (Jenkins and Dai 2021) via increased sensible and latent heat fluxes into the lower atmosphere in winter (Boeke and Taylor 2018; Dai et al. 2019; Feldl et al. 2020; Shaw and Smith 2022).

Although sea ice thinning does not contribute to annual-mean polar amplification or substantial poleward energy transport changes, it does shape the seasonal climate changes. We interpret the suppressed summer warming that occurs in response to sea ice melt as a consequence of latent heat absorption, while winter sea ice thinning causes warming through increasing conductive heat flux. Sea ice thinning thus drives a stronger seasonality of polar warming, consistent with more idealized studies using an energy balance model and gray radiation GCM in Feldl and Merlis (2021) and a single-column sea ice model in Hahn et al. (2022). Furthermore, the seasonal temperature pattern induced by sea ice thinning, which can only be simulated in a sea ice model that includes ice thermodynamics, contributes to seasonality in the dry energy transport changes. A unique aspect of our study is that, by separately locking ice thickness and fraction and locking ice fraction alone, we are able to cleanly isolate and quantify the effect of ice albedo changes and ice thinning on the surface temperature and atmospheric energy transport response across the seasonal cycle.

The water vapor feedback is widely considered a tropical amplification contributor (Pithan and Mauritsen 2014; Goosse et al. 2018; Hahn et al. 2021). However, we find that the poleward latent energy transport induced by enhanced water vapor at lower latitudes contributes to polar amplification. The magnitude of the contribution of increased latent energy transport is comparable to (even slightly larger than) that of the water vapor feedback in our annual mean analysis, leading to a net polar amplification. These results are supported by Beer and Eisenman (2022), who apply a feedback locking method in a moist energy balance model and find that the water vapor feedback becomes the primary factor of polar amplification, due to its interaction with other positive feedbacks. Russotto and Biasutti (2020) also conclude that latent energy transport, interacting with water vapor feedback, plays an essential role in polar amplification. For our seasonal polar warming diagnosis, summer amplification by the water vapor feedback is compensated by its induced increase in poleward latent energy transport, which is larger in winter. Since this mechanism is illuminated by ice-locking simulations, the water vapor feedback is precluded from causing sea ice loss in our diagnostic framework, though, because it warms the polar regions in summer, it may help to initiate the ice-albedo feedback. Notably, sea ice retreat provokes only small changes in latent energy transport in our annual mean and seasonal analysis, with the largest transport increase into the Arctic in late summer (Fig. S3e in the online supplemental material).

The increase in latent energy transport into polar regions in our simulations is largely seasonally invariant. The total response of Arctic transport is composed of a modest winter peak in response to the water vapor radiative effect and a modest late summer peak in response to sea ice retreat (Fig. S3). This suggests that the summer maximum in latent energy transport increases identified in previous studies (McCrystall et al. 2021; Kaufman and Feldl 2022) is associated at least in part with sea ice loss. However, we also note that our idealized aquaplanet configuration includes a 60-m-deep slab ocean and hence has a higher heat capacity than a model with continents. A higher heat capacity leads to a delayed phase shift of the tropical temperature maximum (Dwyer et al. 2012), the tropical moisture maximum (via the Clausius-Clapeyron relation), and all else equal, the midlatitude moisture gradient. In response to the water vapor radiative effect, for instance, a shallower mixed layer would likely produce a somewhat earlier peak in the latent energy transport increase. While this may lead to stronger, summer-dominated seasonality of latent energy transport increase in the total response, we do not expect it to alter our main result that the water vapor radiative effect produces seasonally symmetric polar warming, because the peak water vapor feedback would also be shifted to earlier in the season.

The idealized GCM used in this study does not include a representation of clouds and hence our analysis omits the cloud feedback. Only about half of the literature supports that cloud feedback contributes to polar amplification, while the other half supports that it contributes to tropical amplification or is unsure (Previdi et al. 2021). This uncertainty comes from the complex interaction between clouds and other processes. Low cloud formation by increasing turbulent heat fluxes over the newly exposed ocean enhances the downward longwave flux (Kay and Gettelman 2009), which may lead to stronger polar warming in fall and winter. The condensational heating of clouds by increasing turbulent heat fluxes during winter also mediates the impact of sea ice loss on the vertical structure of Arctic warming (Kaufman and Feldl 2022). Clouds may also enhance the impact of latent energy transport increases through their longwave effect, contributing to winter polar warming (Taylor et al. 2022; Dimitratos et al. 2023). Besides the local impacts, the negative shortwave cloud feedback in the polar region may strengthen the poleward energy transport by increasing the meridional temperature gradient.

In conclusion, we separate the effect of CO₂, water vapor, sea ice retreat, and sea ice thinning to polar amplification in a hierarchy of idealized models. We confirm that the ice-albedo feedback is the primary factor in annual-mean polar warming, ocean heat uptake accounts for the seasonal delay, and the dry atmospheric heat transport is a passive response to surface warming patterns in all cases. Sea ice loss is the essential physical process in shaping the seasonality of polar warming, with about 57% of winter amplification contributed by sea ice retreat and 43% of winter amplification contributed by sea ice thinning (calculated as the distance from the 1:1 line in Figs. 5e,f). Both the water vapor feedback and latent energy transport changes are manifestations of a preferential tropical

and summer hemisphere increase in humidity, with the winter hemisphere experiencing a corresponding increase in the meridional moisture gradient. Thus, the secondary contribution of latent energy transport to annual-mean polar amplification is intrinsic to the tropical amplification effect of the water vapor feedback. Our results highlight the importance of the interaction between feedbacks and atmospheric energy transports on the seasonality polar amplification, and thus improve understanding of its mechanisms.

Acknowledgments. This material is based upon work supported by the National Science Foundation under Award AGS-1753034. We thank Xi Zhang, Timothy Merlis, and Mark England for helpful discussions. Codes for calculating the gray radiation kernels (https://github.com/lxyz/Isca_kernels) and for the RRTM radiative kernels (<https://pyrrtm.flannaghan.com/>) were obtained online. We acknowledge use of the lux supercomputer at the University of California, Santa Cruz, funded by NSF MRI Grant AST-1828315.

Data availability statement. Data and code supporting this study are available online (<https://github.com/pochunchung/Isca>).

REFERENCES

Audette, A., and Coauthors, 2021: Opposite responses of the dry and moist eddy heat transport into the Arctic in the PAMIP experiments. *Geophys. Res. Lett.*, **48**, e2020GL089990, <https://doi.org/10.1029/2020GL089990>.

Baggett, C., and S. Lee, 2017: An identification of the mechanisms that lead to Arctic warming during planetary-scale and synoptic-scale wave life cycles. *J. Atmos. Sci.*, **74**, 1859–1877, <https://doi.org/10.1175/JAS-D-16-0156.1>.

Beer, E., and I. Eisenman, 2022: Revisiting the role of the water vapor and lapse rate feedbacks in the Arctic amplification of climate change. *J. Climate*, **35**, 2975–2988, <https://doi.org/10.1175/JCLI-D-21-0814.1>.

Boeke, R. C., and P. C. Taylor, 2018: Seasonal energy exchange in sea ice retreat regions contributes to differences in projected Arctic warming. *Nat. Commun.*, **9**, 5017, <https://doi.org/10.1038/s41467-018-07061-9>.

—, —, and S. A. Sejas, 2021: On the nature of the Arctic's positive lapse-rate feedback. *Geophys. Res. Lett.*, **48**, e2020GL091109, <https://doi.org/10.1029/2020GL091109>.

Budyko, M. I., 1969: The effect of solar radiation variations on the climate of the Earth. *Tellus*, **21**, 611–619, <https://doi.org/10.1111/j.2153-3490.1969.tb00466.x>.

Dai, A., D. Luo, M. Song, and J. Liu, 2019: Arctic amplification is caused by sea-ice loss under increasing CO₂. *Nat. Commun.*, **10**, 121, <https://doi.org/10.1038/s41467-018-07954-9>.

Deser, C., R. Tomas, M. Alexander, and D. Lawrence, 2010: The seasonal atmospheric response to projected Arctic sea ice loss in the late twenty-first century. *J. Climate*, **23**, 333–351, <https://doi.org/10.1175/2009JCLI3053.1>.

Dimitratos, A., R. Caballero, and A. M. L. Ekman, 2023: Controls on surface warming by winter Arctic moist intrusions in idealized large-eddy simulations. *J. Climate*, **36**, 1287–1300, <https://doi.org/10.1175/JCLI-D-22-0174.1>.

Donohoe, A., K. C. Armour, G. H. Roe, D. S. Battisti, and L. Hahn, 2020: The partitioning of meridional heat transport from the last glacial maximum to CO₂ quadrupling in coupled climate models. *J. Climate*, **33**, 4141–4165, <https://doi.org/10.1175/JCLI-D-19-0797.1>.

Dwyer, J. G., M. Biasutti, and A. H. Sobel, 2012: Projected changes in the seasonal cycle of surface temperature. *J. Climate*, **25**, 6359–6374, <https://doi.org/10.1175/JCLI-D-11-00741.1>.

England, M. R., I. Eisenman, and T. J. W. Wagner, 2022: Spurious climate impacts in coupled sea ice loss simulations. *J. Climate*, **35**, 7401–7411, <https://doi.org/10.1175/JCLI-D-21-0647.1>.

Feldl, N., and G. H. Roe, 2013: The nonlinear and nonlocal nature of climate feedbacks. *J. Climate*, **26**, 8289–8304, <https://doi.org/10.1175/JCLI-D-12-00631.1>.

—, and T. M. Merlis, 2021: Polar amplification in idealized climates: The role of ice, moisture, and seasons. *Geophys. Res. Lett.*, **48**, e2021GL094130, <https://doi.org/10.1029/2021GL094130>.

—, S. Bordoni, and T. M. Merlis, 2017: Coupled high-latitude climate feedbacks and their impact on atmospheric heat transport. *J. Climate*, **30**, 189–201, <https://doi.org/10.1175/JCLI-D-16-0324.1>.

—, S. Po-Chedley, H. K. A. Singh, S. Hay, and P. J. Kushner, 2020: Sea ice and atmospheric circulation shape the high-latitude lapse rate feedback. *npj Climate Atmos. Sci.*, **3**, 41, <https://doi.org/10.1038/s41612-020-00146-7>.

Frierson, D. M. W., I. M. Held, and P. Zurita-Gotor, 2006: A gray-radiation aquaplanet moist GCM. Part I: Static stability and eddy scale. *J. Atmos. Sci.*, **63**, 2548–2566, <https://doi.org/10.1175/JAS3753.1>.

—, —, and —, 2007: A gray-radiation aquaplanet moist GCM. Part II: Energy transports in altered climates. *J. Atmos. Sci.*, **64**, 1680–1693, <https://doi.org/10.1175/JAS3913.1>.

Gosse, H., and Coauthors, 2018: Quantifying climate feedbacks in polar regions. *Nat. Commun.*, **9**, 1919, <https://doi.org/10.1038/s41467-018-04173-0>.

Graversen, R. G., and M. Burtu, 2016: Arctic amplification enhanced by latent energy transport of atmospheric planetary waves. *Quart. J. Roy. Meteor. Soc.*, **142**, 2046–2054, <https://doi.org/10.1002/qj.2802>.

—, and P. L. Langen, 2019: On the role of the atmospheric energy transport in $2 \times \text{CO}_2$ -induced polar amplification in CESM1. *J. Climate*, **32**, 3941–3956, <https://doi.org/10.1175/JCLI-D-18-0546.1>.

—, —, and T. Mauritsen, 2014: Polar amplification in CCSM4: Contributions from the lapse rate and surface albedo feedbacks. *J. Climate*, **27**, 4433–4450, <https://doi.org/10.1175/JCLI-D-13-00551.1>.

Hahn, L. C., K. C. Armour, M. D. Zelinka, C. M. Bitz, and A. Donohoe, 2021: Contributions to polar amplification in CMIP5 and CMIP6 models. *Front. Earth Sci.*, **9**, 710036, <https://doi.org/10.3389/feart.2021.710036>.

—, —, D. S. Battisti, I. Eisenman, and C. M. Bitz, 2022: Seasonality in Arctic warming driven by sea ice effective heat capacity. *J. Climate*, **35**, 1629–1642, <https://doi.org/10.1175/JCLI-D-21-0626.1>.

Hansen, J., and Coauthors, 2005: Efficacy of climate forcings. *J. Geophys. Res.*, **110**, D18104, <https://doi.org/10.1029/2005JD005776>.

Henry, M., T. M. Merlis, N. J. Lutsko, and B. E. J. Rose, 2021: Decomposing the drivers of polar amplification with a single-column model. *J. Climate*, **34**, 2355–2365, <https://doi.org/10.1175/JCLI-D-20-0178.1>.

Holland, M. M., and C. M. Bitz, 2003: Polar amplification of climate change in coupled models. *Climate Dyn.*, **21**, 221–232, <https://doi.org/10.1007/s00382-003-0332-6>.

Hwang, Y.-T., D. M. W. Frierson, and J. E. Kay, 2011: Coupling between Arctic feedbacks and changes in poleward energy transport. *Geophys. Res. Lett.*, **38**, L17704, <https://doi.org/10.1029/2011GL048546>.

Jenkins, M., and A. Dai, 2021: The impact of sea-ice loss on Arctic climate feedbacks and their role for Arctic amplification. *Geophys. Res. Lett.*, **48**, e2021GL094599, <https://doi.org/10.1029/2021GL094599>.

Jucker, M., and E. P. Gerber, 2017: Untangling the annual cycle of the tropical tropopause layer with an idealized moist model. *J. Climate*, **30**, 7339–7358, <https://doi.org/10.1175/JCLI-D-17-0127.1>.

Kaufman, Z. S., and N. Feldl, 2022: Causes of the Arctic's lower-tropospheric warming structure. *J. Climate*, **35**, 1983–2002, <https://doi.org/10.1175/JCLI-D-21-0298.1>.

Kay, J. E., and A. Gettelman, 2009: Cloud influence on and response to seasonal Arctic sea ice loss. *J. Geophys. Res.*, **114**, D18204, <https://doi.org/10.1029/2009JD011773>.

Manabe, S., and R. T. Wetherald, 1975: The effects of doubling the CO₂ concentration on the climate of a general circulation model. *J. Atmos. Sci.*, **32**, 3–15, [https://doi.org/10.1175/1520-0469\(1975\)032<0003:TEODTC>2.0.CO;2](https://doi.org/10.1175/1520-0469(1975)032<0003:TEODTC>2.0.CO;2).

—, and R. J. Stouffer, 1980: Sensitivity of a global climate model to an increase of CO₂ concentration in the atmosphere. *J. Geophys. Res.*, **85**, 5529–5554, <https://doi.org/10.1029/JC085iC10p05529>.

McCrystall, M. R., J. Stroeve, M. Serreze, B. C. Forbes, and J. A. Screen, 2021: New climate models reveal faster and larger increases in Arctic precipitation than previously projected. *Nat. Commun.*, **12**, 6765, <https://doi.org/10.1038/s41467-021-27031-y>.

Mlawer, E. J., S. J. Taubman, P. D. Brown, M. J. Iacono, and S. A. Clough, 1997: Radiative transfer for inhomogeneous atmospheres: RRTM, a validated correlated-k model for the longwave. *J. Geophys. Res.*, **102**, 16 663–16 682, <https://doi.org/10.1029/97JD00237>.

Pithan, F., and T. Mauritsen, 2014: Arctic amplification dominated by temperature feedbacks in contemporary climate models. *Nat. Geosci.*, **7**, 181–184, <https://doi.org/10.1038/ngeo2071>.

Previdi, M., K. L. Smith, and L. M. Polvani, 2021: Arctic amplification of climate change: A review of underlying mechanisms. *Environ. Res. Lett.*, **16**, 093003, <https://doi.org/10.1088/1748-9326/ac1e29>.

Russotto, R. D., and M. Biasutti, 2020: Polar amplification as an inherent response of a circulating atmosphere: Results from the TRACMIP aquaplanets. *Geophys. Res. Lett.*, **47**, e2019GL086771, <https://doi.org/10.1029/2019GL086771>.

Screen, J. A., and I. Simmonds, 2010a: The central role of diminishing sea ice in recent Arctic temperature amplification. *Nature*, **464**, 1334–1337, <https://doi.org/10.1038/nature09051>.

—, and —, 2010b: Increasing fall-winter energy loss from the Arctic Ocean and its role in Arctic temperature amplification. *Geophys. Res. Lett.*, **37**, L16707, <https://doi.org/10.1029/2010GL044136>.

Semtner, A. J., Jr., 1976: A model for the thermodynamic growth of sea ice in numerical investigations of climate. *J. Phys. Oceanogr.*, **6**, 379–389, [https://doi.org/10.1175/1520-0485\(1976\)006<0379:AMFTTG>2.0.CO;2](https://doi.org/10.1175/1520-0485(1976)006<0379:AMFTTG>2.0.CO;2).

Serreze, M. C., A. P. Barrett, J. C. Stroeve, D. N. Kindig, and M. M. Holland, 2009: The emergence of surface-based Arctic amplification. *Cryosphere*, **3**, 11–19, <https://doi.org/10.5194/tc-3-11-2009>.

Shaw, T. A., and Z. Smith, 2022: The midlatitude response to polar sea ice loss: Idealized slab-ocean aquaplanet experiments with thermodynamic sea ice. *J. Climate*, **35**, 2633–2649, <https://doi.org/10.1175/JCLI-D-21-0508.1>.

Shell, K. M., J. T. Kiehl, and C. A. Shields, 2008: Using the radiative kernel technique to calculate climate feedbacks in NCAR's Community Atmospheric Model. *J. Climate*, **21**, 2269–2282, <https://doi.org/10.1175/2007JCLI2044.1>.

Soden, B. J., I. M. Held, R. Colman, K. M. Shell, J. T. Kiehl, and C. A. Shields, 2008: Quantifying climate feedbacks using radiative kernels. *J. Climate*, **21**, 3504–3520, <https://doi.org/10.1175/2007JCLI2110.1>.

Stuecker, M. F., and Coauthors, 2018: Polar amplification dominated by local forcing and feedbacks. *Nat. Climate Change*, **8**, 1076–1081, <https://doi.org/10.1038/s41558-018-0339-y>.

Taylor, K. E., M. Crucifix, P. Braconnot, C. D. Hewitt, C. Doutriaux, A. J. Broccoli, J. F. B. Mitchell, and M. J. Webb, 2007: Estimating shortwave radiative forcing and response in climate models. *J. Climate*, **20**, 2530–2543, <https://doi.org/10.1175/JCLI4143.1>.

Taylor, P. C., M. Cai, A. Hu, J. Meehl, W. Washington, and G. J. Zhang, 2013: A decomposition of feedback contributions to polar warming amplification. *J. Climate*, **26**, 7023–7043, <https://doi.org/10.1175/JCLI-D-12-00696.1>.

—, and Coauthors, 2022: Process drivers, inter-model spread, and the path forward: A review of amplified Arctic warming. *Front. Earth Sci.*, **9**, 758361, <https://doi.org/10.3389/feart.2021.758361>.

Vallis, G. K., and Coauthors, 2018: Isca, v1.0: A framework for the global modelling of the atmospheres of earth and other planets at varying levels of complexity. *Geosci. Model Dev.*, **11**, 843–859, <https://doi.org/10.5194/gmd-11-843-2018>.

Yoshimori, M., A. Abe-Ouchi, and A. Laîné, 2017: The role of atmospheric heat transport and regional feedbacks in the Arctic warming at equilibrium. *Climate Dyn.*, **49**, 3457–3472, <https://doi.org/10.1007/s00382-017-3523-2>.

Zhang, X., T. Schneider, Z. Shen, K. G. Pressel, and I. Eisenman, 2022: Seasonal cycle of idealized polar clouds: Large eddy simulations driven by a GCM. *J. Adv. Model. Earth Syst.*, **14**, e2021MS002671, <https://doi.org/10.1029/2021MS002671>.